

AEMIP robust inversion using maximum phase angle Cole–Cole model re-parameterisation applied for HTEM survey over Lamego gold mine, Quadrilátero Ferrífero, MG, Brazil

Marco Antonio Couto Junior, Gianluca Fiandaca, Pradip Kumar Maurya, Anders Vest Christiansen, Jorge Luís Porsani & Esben Auken

To cite this article: Marco Antonio Couto Junior, Gianluca Fiandaca, Pradip Kumar Maurya, Anders Vest Christiansen, Jorge Luís Porsani & Esben Auken (2019): AEMIP robust inversion using maximum phase angle Cole–Cole model re-parameterisation applied for HTEM survey over Lamego gold mine, Quadrilátero Ferrífero, MG, Brazil, Exploration Geophysics, DOI: [10.1080/08123985.2019.1682458](https://doi.org/10.1080/08123985.2019.1682458)

To link to this article: <https://doi.org/10.1080/08123985.2019.1682458>



Published online: 31 Oct 2019.



Submit your article to this journal [↗](#)



View related articles [↗](#)



View Crossmark data [↗](#)



AEMIP robust inversion using maximum phase angle Cole–Cole model re-parameterisation applied for HTEM survey over Lamego gold mine, Quadrilátero Ferrífero, MG, Brazil

Marco Antonio Couto Junior ^{a,b}, Gianluca Fiandaca^c, Pradip Kumar Maurya^c, Anders Vest Christiansen ^c, Jorge Luís Porsani^b and Esben Auken ^c

^aGeological Survey of Brazil (CPRM), Belo Horizonte Regional Office, Geology and Mineral Resources Management, Belo Horizonte, Brazil;

^bDepartamento de Geofísica, Universidade de São Paulo (USP), Instituto de Astronomia, Geofísica e Ciências Atmosféricas (IAG), São Paulo, Brasil; ^cHydrogeophysics Group (HGG), Department of Geosciences, Aarhus University (AU) Aarhus C, Denmark

ABSTRACT

This paper presents the results of airborne electromagnetic induced polarisation inversions using the Maximum Phase Angle (MPA) model for a helicopter time domain survey in the Quadrilátero Ferrífero area, Minas Gerais State (MG), Brazil. The inversions were conducted using a laterally constrained robust scheme, in order to decrease the difficulties to recover the multi-parametric model in a very ill-posed inverse problem, often found in induced polarisation studies. A set of six flight lines over the Lamego gold mine mineralised structure were inverted using the MPA re-parameterisation of the Cole–Cole model and also the classical resistivity-only parameterisation, in order to understand the implications of the induced polarisation effect in the data and, consequently, in the resistivity model. A synthetic study was also conducted, seeking to understand what to expect from the resistivity-only inversions in the real data. According to borehole lithological data and previous structural knowledge from the literature, the results from the Maximum Phase Angle approach indicate an important chargeable body that seems to be in good agreement with a sulfide enriched carbonaceous/graphite and altered mafic units, which are important markers for the gold mineralisation.

ARTICLE HISTORY

Received 30 August 2018

Accepted 1 October 2019

KEYWORDS

Airborne electromagnetics; induced polarisation; maximum phase angle

Introduction

During the last decade, the interest to model airborne electromagnetic induced polarisation (AEMIP) phenomena has significantly increased (Kang and Oldenburg 2016; Kratzer and Macnae 2012; Macnae 2016; Marchant, Haber, and Oldenburg 2014; Viezzoli, Fiandaca, and Sergio 2013). Due to the improvements of the helicopter transient electromagnetic (HTEM) systems in power and resolution, like the newest SkyTEM312HP (Gisselø and Nyboe 2018) and VTEMTM *super max* (<http://geotech.ca/>) systems, these studies were mainly motivated by applications in mineral exploration, groundwater and environmental studies (Kaminski and Viezzoli 2017; Kang, Fournier, and Oldenburg 2017; Viezzoli, Kaminski, and Fiandaca 2017; Viezzoli et al. 2016). In particular, for mineral exploration, it has potential to survey and characterise economic mineralizations related to disseminated sulfide zones, especially within deposits associated with hydrothermal and igneous processes. The use of AEMIP can help to decrease ambiguities between mineralizations and their host rocks, to understand the structural control

and their association with chemical traps, like reactive carbonaceous units in highly hydrothermal altered terrains. In addition, AEMIP may be useful in some circumstances to map large areas with chargeability information in a very short time compared to ground-based induced polarisation (IP) surveys. Covering large areas with ground-based IP methods usually present difficulties in accessibility, logistics and costs.

Although the newest powerful HTEM systems are superior in observing the AEMIP phenomenon, there are many existing airborne electromagnetic (AEM) surveys carried out with less powerful systems, which also contain IP effects. These data should be investigated for IP information, in order to provide preliminary information for new IP studies to be carried out in the same area and/or improve the resistivity and chargeability models. With this philosophy in mind, we present an AEMIP modelling study in the Lamego gold mine (AngloGold Ashanti property), in the Greenstone Belt Rio das Velhas, Quadrilátero Ferrífero (QF) area, Minas Gerais State (MG), Brazil, using data acquired with an AeroTEM^{HD} system. The survey was flown with N45W orientation,

CONTACT Marco Antonio Couto Junior  marco.couto@cprm.gov.br, marco.couto@usp.br  Geological Survey of Brazil (CPRM), Belo Horizonte Regional Office, Geology and Mineral Resources Management, Brasil Avenue, 1731, 5th floor, Funcionários, Belo Horizonte, MG 30140-002, Brazil; Departamento de Geofísica, Universidade de São Paulo (USP), Instituto de Astronomia, Geofísica e Ciências Atmosféricas (IAG), Rua do Matão, 1226, São Paulo 05508-090, Brasil

250 m flight-line spacing and with total 3560 line-km. This HTEM system has a triangular pulse current waveform, with a peak moment of 711000 NIA and 17 off-time channels for the vertical component.

Due to the high resistive terrain of the greenstone belt, a very urbanised environment associated with mines and cities in the surroundings and a system with a low magnetic moment, the AEM data display several couplings to man-made structures and low signal-to-noise ratios in many parts of the survey. For these reasons it was challenging to find clear AEMIP anomalies. Nevertheless, some sign reversals (negative late time gates) and rapidly decaying dB/dt signals were recorded over the mineralised structure in Lamego mine area. Carbonaceous and graphite schists, associated with gold mineralisation within disseminated metallic sulfides, occur in the mine area, which might be responsible for the IP effects in the AEM data. Indeed, the frequency-domain IP measurements conducted in the laboratory by Smith et al. (1983) on similar lithologies (from a greenstone belt environment in Saudi Arabia) show significant IP effects over the whole measurement range from 0.06 to 1024 Hz.

The AEMIP modelling was conducted on six flight lines over Lamego structure using the 1D laterally constrained robust inversion scheme proposed by Fian-daca et al. (2018a) and Lin et al. (2019), using the Maximum Phase Angle (MPA) re-parameterisation of the Cole–Cole model (Fiandaca, Madsen, and Maurya 2018b) in order to reduce the correlation of the inversion parameters. In addition, the electrical resistivity models obtained through this approach were compared with the ordinary resistivity-only (RO) inversion, in order to understand the differences in the models, with and without IP modelling. All the results were integrated with borehole lithological data. The final result is an integration of all inverted sections in a 3D visualisation of the polarisable body.

Area of study

Lamego is one the most important gold mines in the Quadrilátero Ferrífero (QF) area, MG, Brazil, which is property of AngloGold Ashanti. It is characterised by an Archean orogenic gold deposit, within the rocks of the Rio das Velhas greenstone belt, in the North portion of the QF area. Structurally, the mine is characterised by a reclined, isoclinal and cylindrical fold (Martins et al. 2016) – Figure 1. Lithologically, it is characterised by a metamorphosed volcano-sedimentary sequence composed by mafic units, banded iron formation (BIF)/chert units and carbonaceous/micaceous schists.

According to Martins et al. (2016) and based on borehole data, the gold mineralisation is associated with disseminated sulfides (mainly pyrite, arsenopyrite, chalcopyrite and sphalerite) that are classified in three groups: (i) The quartz-carbonate/sulfides veins crosscut

all lithologies, but with a better development within the BIF layers, with locally stockwork structure; (ii) The Fe-carbonate replacement for sulfides within the BIF layers, which confines the sulfides in this lithology; and (iii) Dissemination within the mafic units and carbonaceous metapelites/schists. The gold grade for each of these mineralisation groups vary between 1.6–15.8 ppm, 0.03–6.63 ppm and 0.03–3.8 ppm, respectively.

Laboratory petrophysical data from lithological borehole samples were used as guidance to define the initial values for the input parameters in the inversion process. These data indicated a very resistive environment ($> 1000 \Omega \text{ m}$ for the mafic unities, reaching values greater than $5000 \Omega \text{ m}$ in the micaceous metapelite zones) associated with the micaceous metapelite and mafic-ultramafic unities, but with conductive and chargeable zones that could be associated with the carbonaceous/graphite metapelites/schists and disseminated sulfides within both carbonaceous and mafic layers, which are an important guide to map the gold mineralisation. It is expected that the IP effect might be generated mainly from these carbonaceous/graphite units, according to petrophysical data from Anglo Gold Ashanti, which presents average values for resistivity and chargeability for the lithological units in Lamego area. In fact, we observed very steep decays often associated with negative transients over Lamego structure. Furthermore, in this work, the IP methodology is used in order to try to define these carbonaceous units, that could be associated as a structural guidance for the gold mineralisation.

HTEM survey and system description

The HTEM system used in the survey in QF region was the Aeroquest AeroTEM^{HD}, with 30 Hz base frequency triangular pulse waveform. The survey flight lines were oriented to NW-SE (azimuth 135) and the spacing between the lines was 250 m. The nominal terrain clearance was 30 m for the EM transmitter/receiver system, it covered 3560 line-km and had a nominal flight speed of 75 km/h with a data reading every 1.5–2.5 m (10 samples/s) along the flight line.

Although the AeroTEM^{HD} system is able to conduct measurements with X (flight line direction) and Z (vertical direction) components receiver coils, only the Z component was used in this work, due the high noise level of the X component. The EM system characteristics are summarised in Table 1, which is based on the information of the survey report and from the data files provided by the contractor.

Methodology

Cole–Cole maximum phase angle model

In this work, the methodology used for the forward calculations of the AEMIP effect is based on the MPA

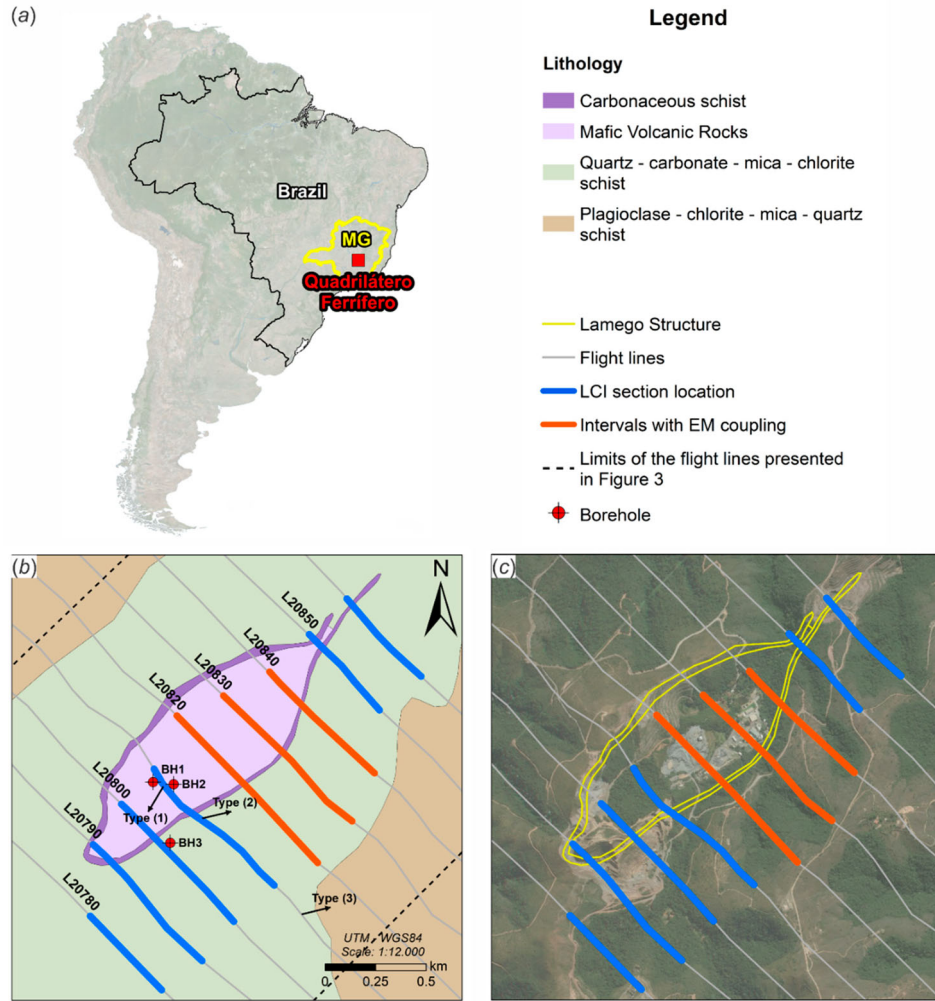


Figure 1. Area of study location. (a) Quadrilátero Ferrífero (QF) location in Brazil and Lamego gold mine. (b) Detailed geological map of Lamego gold mine structure with flight line positions (grey lines, with their number indicated) – the borehole lithological data are indicated by the red points and the LCI sections used in this work are indicated by the blue lines along the flight lines, the orange lines indicate intervals with low signal amplitude and couplings, which are disabled in the inversion analysis. Types (1), (2) and (3) position indicate the types of soundings presented in the Figure 2. The dashed lines indicate the spatial limits of all flight lines presented in this Figure 2. (c) Satellite image over Lamego Mine area, with the indication of the flight lines and the mine infrastructure buildings which caused the coupling in the orange lines intervals.

Table 1. AeroTEM^{HD} system description summary for QF area (based on survey report and data files provided by Aeroquest).

	Parameter	Value
Transmitter	Loop diameter	20 m
	Peak current	323 A
	Peak moment	711,000 NIA
	Repetition frequency	30 Hz
	Turn-on time	-4,476 μ s
	Peak current time	-2,133 μ s
	Turn-off time (when 0 current is reached) ^a	0
	Waveform	Triangular
Receiver	Sample rate ^a	10 Hz
	Number of gates (only off-time used)	17
	Time gates interval (off-times) ^b	8.75 μ s to 9,532 μ s

^aAfter on-survey processing.

^bTime values related with the opening of the gates and referenced to the turn-off time.

re-parameterisation of the Cole–Cole Model, introduced by and implemented in AarhusInv. The MPA is a re-parameterisation of the frequency dependent

complex resistivity for the Cole–Cole model (CC), as defined by (Pelton et al. 1978):

$$\tilde{\rho}(\omega) = \rho_0 \left[1 - m_0 \left(1 - \frac{1}{1 + (i\omega\tau_\rho)^C} \right) \right] \quad (1)$$

where $\rho_0 = \tilde{\rho}(\omega = 0)$ is the direct current resistivity, m_0 is the intrinsic chargeability as described in (Seigel 1959), τ_ρ is the relaxation time, C is the frequency dependency parameter, $\omega = 2\pi f$ is the angular frequency for the frequency f , and $i = \sqrt{-1}$ is the imaginary unit.

As demonstrated by Fiandaca, Madsen, and Maurya (2018b) and Lin et al. (2019), the MPA re-parameterisation reduces the correlations between the model parameters and provides models with better resolution in comparison with the classical CC model, especially for low C values. The MPA uses the following model parameters:

$$\mathbf{m}_{\text{MPA}} = \{\rho_0, \phi_{\text{max}}, \tau_\phi, C\} \quad (2)$$

where ρ_0 and C are the same parameters of the CC model in Equation (1), ϕ_{\max} is the maximum phase angle of the CC complex conductivity (i.e. the minimum of the complex resistivity phase) and τ_ϕ is the relaxation time associated with the frequency ($f = 1/2\pi\tau_\phi$) where ϕ_{\max} is reached. The relation between τ_ρ and τ_ϕ is given by (Fiandaca, Madsen, and Maurya 2018b):

$$\tau_\phi = \tau_\rho(1 - m_0)^{1/2C} \quad (3)$$

The use of the maximum phase of the complex conductivity in the inversion model, instead of the m_0 parameter of the classic Cole–Cole model, simplify the comparison with ancillary IP data, which are often phase spectra measured in the frequency domain in the laboratory on rock samples.

1D Laterally constrained robust inversion scheme for induced polarization data

In this work, all AEMIP inversions were conducted using the 1D laterally constrained inversion (LCI) robust scheme proposed by Lin et al. (2019). This approach helps addressing the significant ill-posedness of a multi-parametric AEMIP inversion and recovers the MPA parameters in Equation (2) properly. The LCI scheme minimises an objective function with 2D lateral constraints on the model parameter space, given by:

$$Q = \left(\frac{\delta \mathbf{d}^T \mathbf{C}_{\text{obs}}^{-1} \delta \mathbf{d} + \delta \mathbf{r}^T \mathbf{C}_R^{-1} \delta \mathbf{r}}{N_d + N_R} \right) \quad (4)$$

where $\delta \mathbf{d} = \mathbf{d} - \mathbf{d}_{\text{obs}}$ is the difference between the forward response \mathbf{d} and the observed data \mathbf{d}_{obs} ; $\delta \mathbf{r} = -\mathbf{Rm}$ is the roughness of the model vector parameter \mathbf{m} , and \mathbf{R} is the roughness matrix; \mathbf{C}_{obs} and \mathbf{C}_R are the covariance matrices related to the data and constraints, respectively; and N_d and N_R are the numbers of data points and roughness constraints, respectively.

Using the LCI technique, the key points of the robust inversion scheme is summarised by the following steps (for a detailed description of this technique, we address the work of Lin et al. 2019):

- (1) Model re-parameterisation using the Cole–Cole MPA approach;
- (2) Definition of a robust initial resistivity model through inversions of positive-only data using very tight spatial constraints. The initial models for the other parameters were defined manually. In this work, the initial values for ϕ_{\max} was 300 mrad, similar to the phase range based on the analogous lithologies presented in Smith et al. (1983), and τ_ϕ and C started from 0.001 s to 0.5, respectively.
- (3) Locking of τ_ϕ and C for the first few (here five) iterations, to build structure in the resistivity and chargeability domains first.

- (4) Increasing the data standard deviation around the sign change in the dB/dt decay curve.
- (5) Modification of the damping scheme allowing for individual damping of the different parameters, which improves the balance of the multi-parameter model space.

Data processing and anomaly selection

The preliminary data processing includes the standard automatic processing of voltage and altitude data, followed by manual processing, as described in (Auken et al. 2009). The automatic data processing was done in Aarhus Workbench (www.aarhusgeosoftware.dk) seeking the best preservation (compared to raw data) of the negative transients in the late times for AeroTEM^{HD} system by having limited lateral averaging and no slope filtering. The slope filtering was disabled to keep fast decaying signals arising from the IP effects. A manual processing step followed the automatic step as the signal-to-noise ratio was very low and many subtle details were close to the noise level. This manual processing was conducted similarly to the workflow described in Kaminski and Viezzoli (2017), in which we conducted a visual inspection of the data throughout the flight lines, in order to identify the very steep dB/dt decays and negative transients associated with the IP effect that may occur over the carbonaceous units, removing the data below the noise level.

Due the poor signal-to-noise ratio at the Lamego mine area, and some flight-line intervals were affected by couplings due to the proximity to the mine infrastructure (indicated in Figure 1(c)). The flight lines that were not used due the poor signal-to-noise ratios and the intervals that present significant couplings are represented as grey and orange line intervals in Figure 1(b) and (c). The poor signal-to-noise ratio in the grey marked might be explained by a highly resistive micaeous metapelite associated with a mafic-ultramafic environment, indicated by the dark and light brown in Figure 1(b), and also due to couplings caused by the highly urbanised surroundings. Despite the generally low signal-to-noise ratio of the dataset, it is still possible to distinguish a clear electromagnetic (EM) anomaly over the Lamego structure, indicating lithological changes in association with the carbonaceous metapelites, BIFs and sulfide layers, as indicated in Figure 2(a) and (b). Figure 2(c) presents the three types of decay curves (raw data) that occur in the area: (1) the ones that could be associated with a typical IP response, (2) not very significant or less evident IP effect, and (3) the noisy data outside the Lamego structure. Type 3 soundings are in the grey flight line intervals refers to resistive lithological units and/or coupled data, which were not used in this work.

In Figure 2(b) it is also noted that even inside the Lamego structure (Figure 1(b)), it is possible to

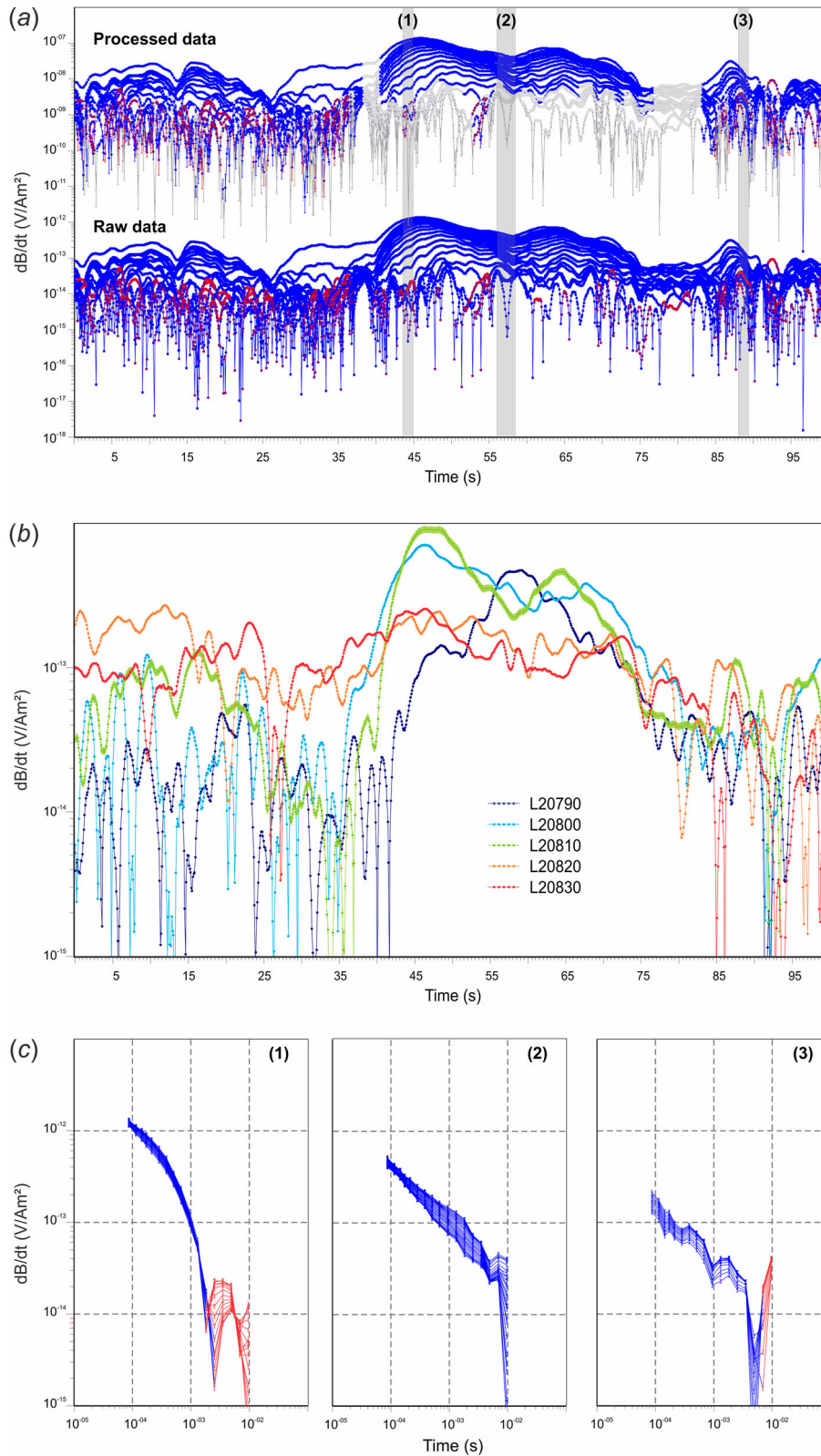


Figure 2. (a) Comparison between raw and processed data for the anomaly over the Lamego structure with indication of anomaly types (1) with IP effect, (2) with not so evident or not presented IP effect and (3) within the very low signal-to-noise ratio area and possibly coupled (not used). The sounding positions along the flight line are also indicated in Figure 1(b) – the processed data are shifted from the raw data by a factor of $\times 10^5$ for clarity and the vertical black dashed lines indicate the interval presented in Figure 3. (b) Comparison between transient anomalies over the Lamego structure along the axial plane direction (NE-SW) showing the decrease in amplitude of the fifth time-channel window at 2.125×10^{-4} s (vertical component in the off-times) in the central part of the structure (L20820 and L20830). (c) Types (1), (2) and (3) dB/dt decays for raw data, as indicated in Figures 1(b) and 2(a).

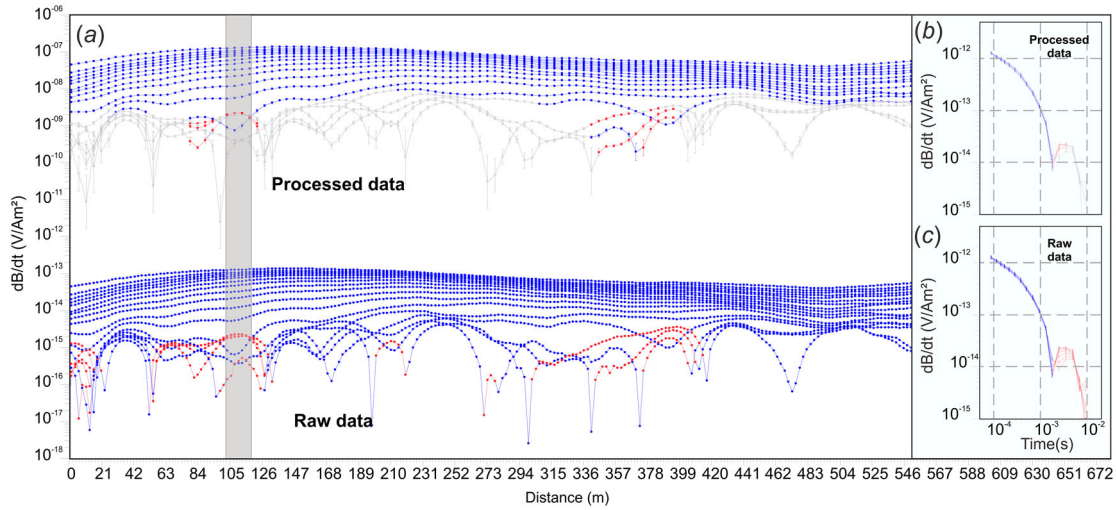


Figure 3. Interval detailed indicated by the vertical black dashed line in Figure 2(a). (a) Processed and raw data for this interval. The vertical grey rectangle indicates the set of soundings showing the typical dB/dt decay with IP effect in Lamego Mine for the (b) processed data and for the (c) raw data.

distinguish a contrast in the EM anomaly along the axial plane direction of the fold structure. The characteristic anomaly starts to appear close to the hinge zone in the NW portion of the structure (flight lines L20790, L20800 and L20810, blue and green lines in Figure 2(b)), the amplitude decreases in the central part (flight lines L20820, L20830, orange and red lines in Figure 2(b)) and increases again in the limb junction in the NE portion of the structure. A very small signal level is observed over the Lamego structure in flight lines L20820, L20830 and L20840 (orange lines intervals in Figure 1(b) and (c)) and these data are not used. In summary, six flight-line intervals with either distinguishable negative transients and/or over-steep slopes of the transient decays were selected for the MPA and RO inversions analysis and geological interpretation (blue lines in Figure 1(b) and (c)), which is presented in the next section.

Finally, Figure 3(a) presents the detailed interval indicated by the vertical dashed lines in Figure 2(a), with a presentation of the typical dB/dt decay affected by IP effects, for both processed (Figure 3(b)) and raw data (Figure 3(c)). When IP effects are present and trigger negative data the absolute signal level will be higher and often above the noise floor where data without sign changes are below the noise level at late times. Though, the noise level is often very hard to detect in the data sections as the data has been pre-processed by the contractor with a lateral smoothing filter to produce the

“raw” data presented in Figure 3(a), bottom. Any decays that are only positive, but increase at late times have been culled.

Results

MPA and RO synthetic modelling for a polarizable subsurface

Based on borehole lithological description and borehole petrophysical data (mean values for the lithological units) we generated synthetic MPA models and the corresponding transient electromagnetic (TEM) data for the AeroTEM^{HD} system. The synthetic data were inverted using the resistivity-only (RO) and MPA parameterizations, for a 3-layer model representing the typical lithological environment in the study area. The reference model used for the synthetic data is summarised in Table 2. It consists of a resistive and non-polarisable upper layer, a conductive and polarisable intermediate layer, and the third resistive non-polarisable layer. The layers lithological relevance is stated in the table as well.

Using the AarhusInv code (Auken et al. 2015) and with the configuration for the AeroTEM^{HD} system described in Table 1, also using the parameters presented in Table 2, we simulated four scenarios considering the increment in the ϕ_{max} value of the second layer from 10 to 500 mrad, i.e. gradually making

Table 2. 3-layer model physical parameters for synthetic modelling.

Layer	ρ_0 ($\Omega \cdot m$)	ϕ_{max} (mrad)	τ_ϕ (ms)	C	Thickness (m)	Lithological Interpretation
1	1000	10	0.1	0.5	70	Metamafic rocks and/or sericitization alteration zones over mafic or felsic rocks (micaceous pelite)
2	300	10–500	10	0.5	300	Carbonaceous/graphite schists and/or carbonatic metapelite with graphite (Carbonate-quartz-sericite schists with carbonaceous material), which could present disseminated sulfides
3	1800	10	0.1	0.5	–	Metamafic volcanic rocks

The thicknesses and resistivity values were based on borehole lithological and petrophysical average values data from AngloGold Ashanti and the IP parameters were based in the preliminary inversions of the AeroTEM^{HD} and reference values from Smith et al. (1983).

the intermediate conductive layer more polarisable and analyzing how well the RO and MPA inversions recover the true model by 1D smooth inversions. The parameters values for each parameter presented in Table 2 were decided based on the values achieved in the preliminary inversion results for the AeroTEM^{HD} data, based on the laboratory petrophysical frequency-domain IP measurements presented in Smith et al. (1983) for similar lithologies in a greenstone belt environment in Saudi Arabia and also data from borehole information for the resistivities values. In particular, in Smith et al. (1983) phase values between 100 and 350 mrad were measured in the frequency interval between 100 and 1000 Hz. A standard deviation of 5% was assigned to each gate of the forward response, but no perturbation was introduced, to focus only in the understanding of the differences responses between RO and MPA models, not considering any other effect in the synthetic

data, like noise level and couplings. The 1D inversions were carried out using a 30-layer smooth model, using the L2 norm for the vertical constraints for both MPA and RO inversions. All RO inversions were conducted removing the negative gates and the last gate before the first negative gate. The MPA inversions were conducted considering all the 17 gates in the off-times for the AeroTEM^{HD} system.

Figure 4 presents the comparison between the inverted resistivity models for RO and the MPA parameterizations for the model described in Table 2. It is noticed that all the RO and MPA inverted models, in all scenarios, fit the data very well and recover a middle conductive layer. However, even though all inverted models fit the data well, there are significant discrepancies between the results of the two inversion approaches. All MPA results recovered the resistivity model with better agreement with the true model,

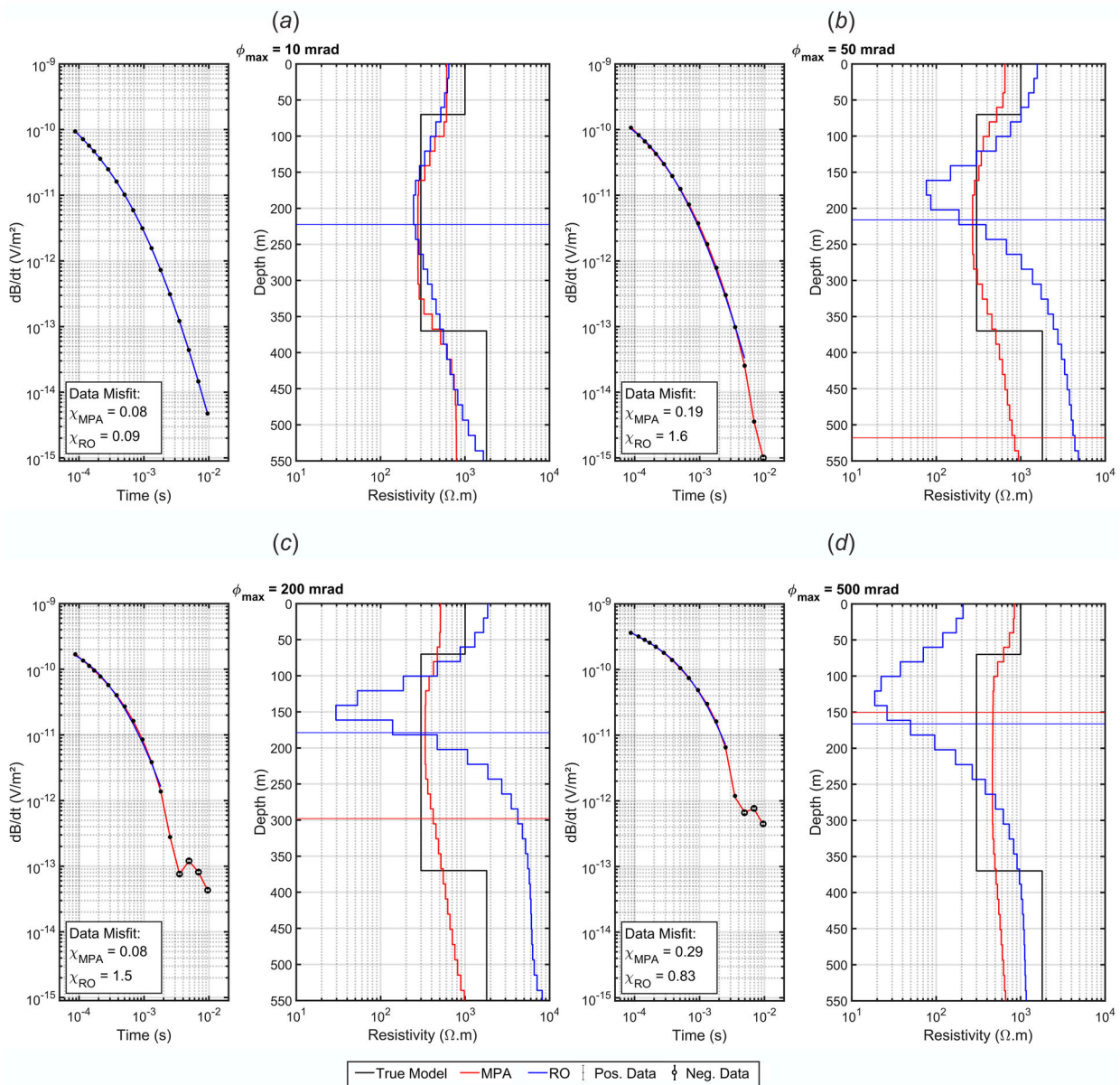


Figure 4. MPA and RO inversion of synthetic 1D TEM data with IP. (a) $\phi_{\max} = 10 \text{ mrad}$, (b) $\phi_{\max} = 50 \text{ mrad}$, (c) $\phi_{\max} = 200 \text{ mrad}$ and (d) $\phi_{\max} = 500 \text{ mrad}$. DOIs are represented by the horizontal continuous lines, according to the models colours.

while the RO inversions generally fail to accurately reproduce the true models.

In the first scenario ($\phi_{\max} = 10$ mrad, Figure 4(a)), the resistivity model is recovered for both MPA and RO smooth models decently. As ϕ_{\max} increases, the conductive layer becomes more conductive and thinner in comparison to the true model and the top boundary of this layer appears deeper (values until 200 mrad, Figure 4(a–c)) or shallower (for 500 mrad, Figure 4(d)); the bottom of the layer remains always shallower than the true model. For all inverted models, the depth of investigation (DOI) was estimated following Fiandaca, Christiansen, and Auken (2015). The DOI values for RO inversion models suggest that there is very limited sensitivity to distinguish the bottom of the conductive layer. On the other hand, the MPA resistivity models have a good agreement with the true model, underlining that this parameterisation approach recovers a more reliable resistivity model. Also, the other MPA parameters are well recovered in the inversions (results not shown in figures for brevity).

In the results presented in Figure 4, the increment in ϕ_{\max} values also causes changes in the amplitude and slope of the transient decay curves before the negative part. In general, the amplitude of the dB/dt curve is

increased and the slope is flatter in the early times and steeper in the time values closer to the sign change. This decay curve behaviour also explains the distortion in the resistivity model for the RO parameterisation. Due to the RO limitations to fit the steep slope of the decay close to the sign change (which is not the case for MPA), the resulting model is made more extreme with a shallower top boundary for the bottom resistor layer and a more conductive and shallower intermediary conductor.

The next section presents the results for the AeroTEM^{HD} real data over the Lamego structure, which presents similar decay behaviour and results as seen in the synthetic tests.

Inversion results of the field data

The 1D laterally constrained inversions (LCI) using RO and MPA models were conducted for all the blue flight-line intervals shown in Figure 1(b) and (c). Figures 5 and 6 show RO and robust MPA inversion results of a representative section for flight line L20810. For all robust MPA inversions, the starting values for the IP parameters were $\phi_{\max} = 300$ mrad, $\tau_{\phi} = 1$ ms and $C = 0.5$.

In Figure 5(a), for the North-West portion of the section, the RO inversion shows in general a three-layer

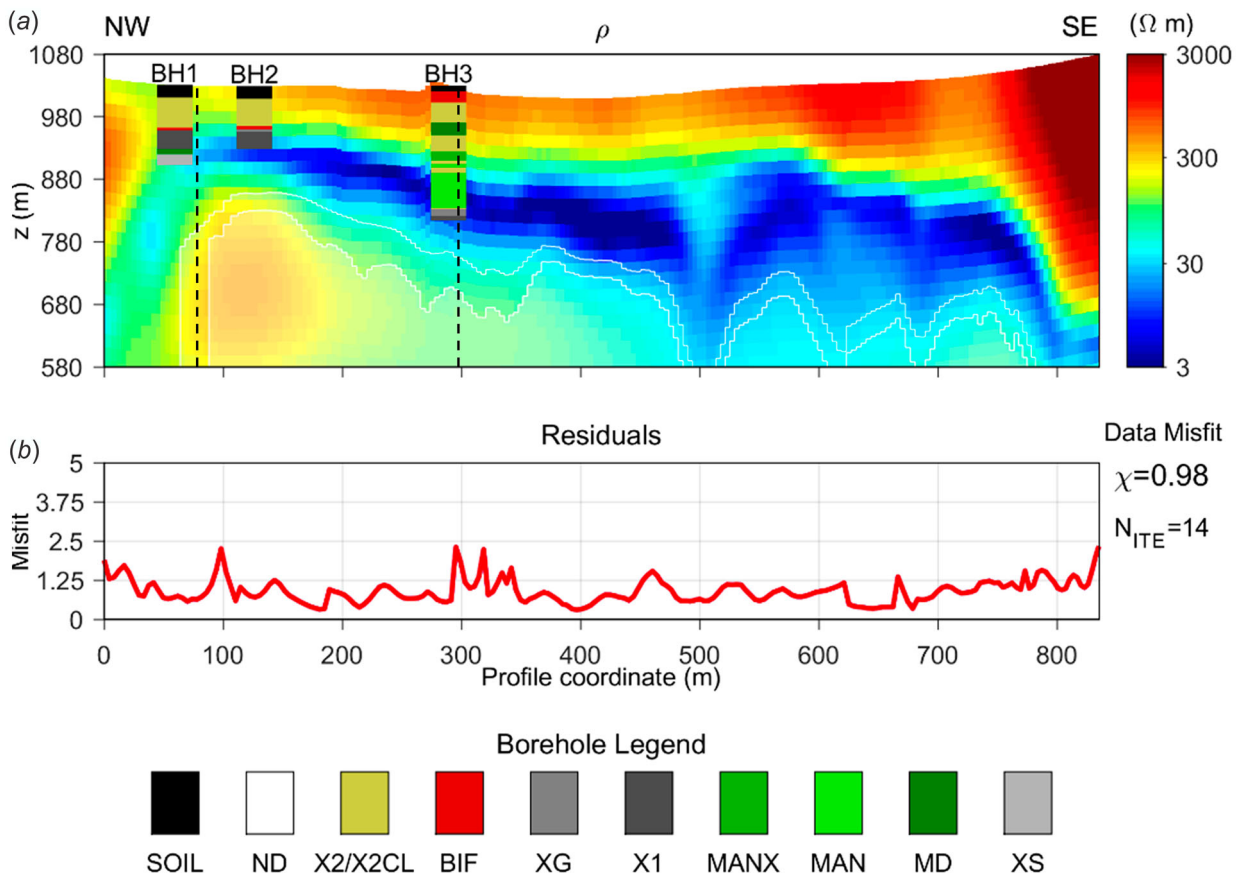


Figure 5. Resistivity-only LCI for flight line L20810 interval over the Lamego structure. (a) Resistivity section. (b) Data misfit. In the borehole lithological legend: SOIL is the soil layer, ND is the non-described interval, X2/X2CL is the micaceous metapelite, BIF represents the banded iron formation layers, XG is the carbonaceous-graphite schists, X1 is the metapelite enriched with carbonaceous material, MAN is the metabasalt/metandesite, MANX is the MAN interval with chloritization alteration, MD is the metadiabase layer and XS is the altered felsic metavolcanoclastic layer. The vertical dashed lines represent the positions of the sounding 19 and 74.

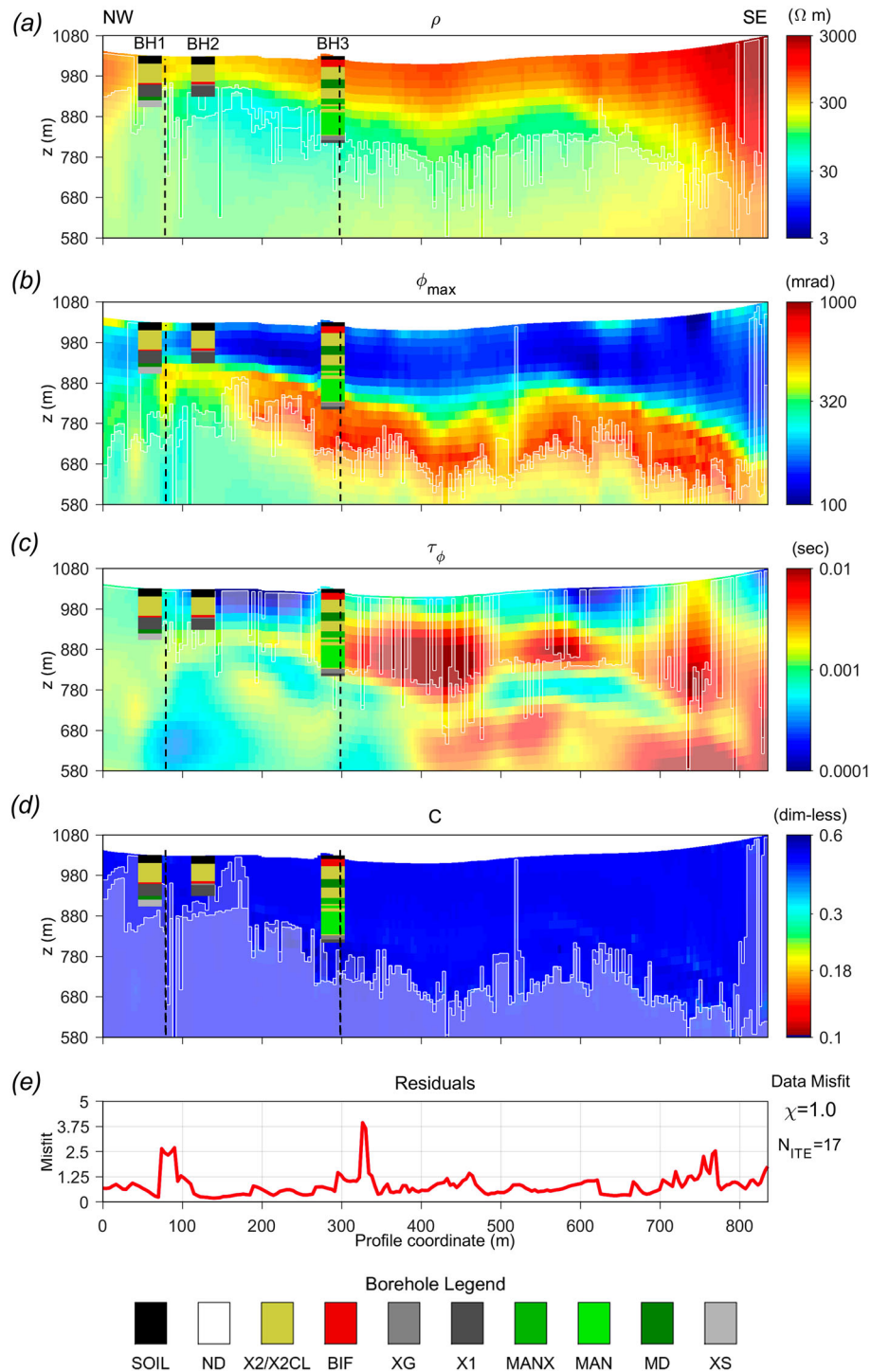


Figure 6. MPA LCI for flight line L20810 interval over the Lamego structure. (a) Resistivity section. (b) ϕ_{\max} section. (c) τ_{ϕ} section. (d) C section. (e) Residuals. The borehole description is associated with the borehole legend presented in Figure 4. The vertical dashed lines represent the positions of the sounding 19 and 74.

model above DOI that consists of a shallow resistive ($> 200 \Omega$ m) layer, a conductive intermediate layer ($< 30 \Omega$ m), and a deep resistor ($> 150 \Omega$ m). The South-East portion of the section show only a two-layer model with a thick and very resistive ($> 1000 \Omega$ m) layer down to ~ 400 m underlain by the intermediate conductive layer, which can be seen throughout the section.

The resistivity model of the MPA inversion (Figure 6(a)) presents a similar resistivity model, but overall with

higher resistivity values and with the absence of the deep resistor below the conductive layer in the North-western portion of the profile. Furthermore, the vertical boundaries in top ~ 100 m of the MPA model agree better with the depth intervals for the micaceous schist in the borehole lithological data (BH1, BH2 and BH3, also indicated in Figure 1(b) and (c)), when compared to the RO inversion result. This is especially evident in the NW portion of the profile, which becomes shallower and more conductive in the RO inversion. The differences

between the resistivity sections in Figures 5(a) and 6(a) indicate that the IP effect cause an important influence in the dataset, and, consequently, in the way the RO inversions respond to it.

Concerning about the possibility to avoid the IP effect in RO inversions, it might be argued that if more late gates are removed in data processing, seeking to avoid the very steep decays of the dB/dt curves, the

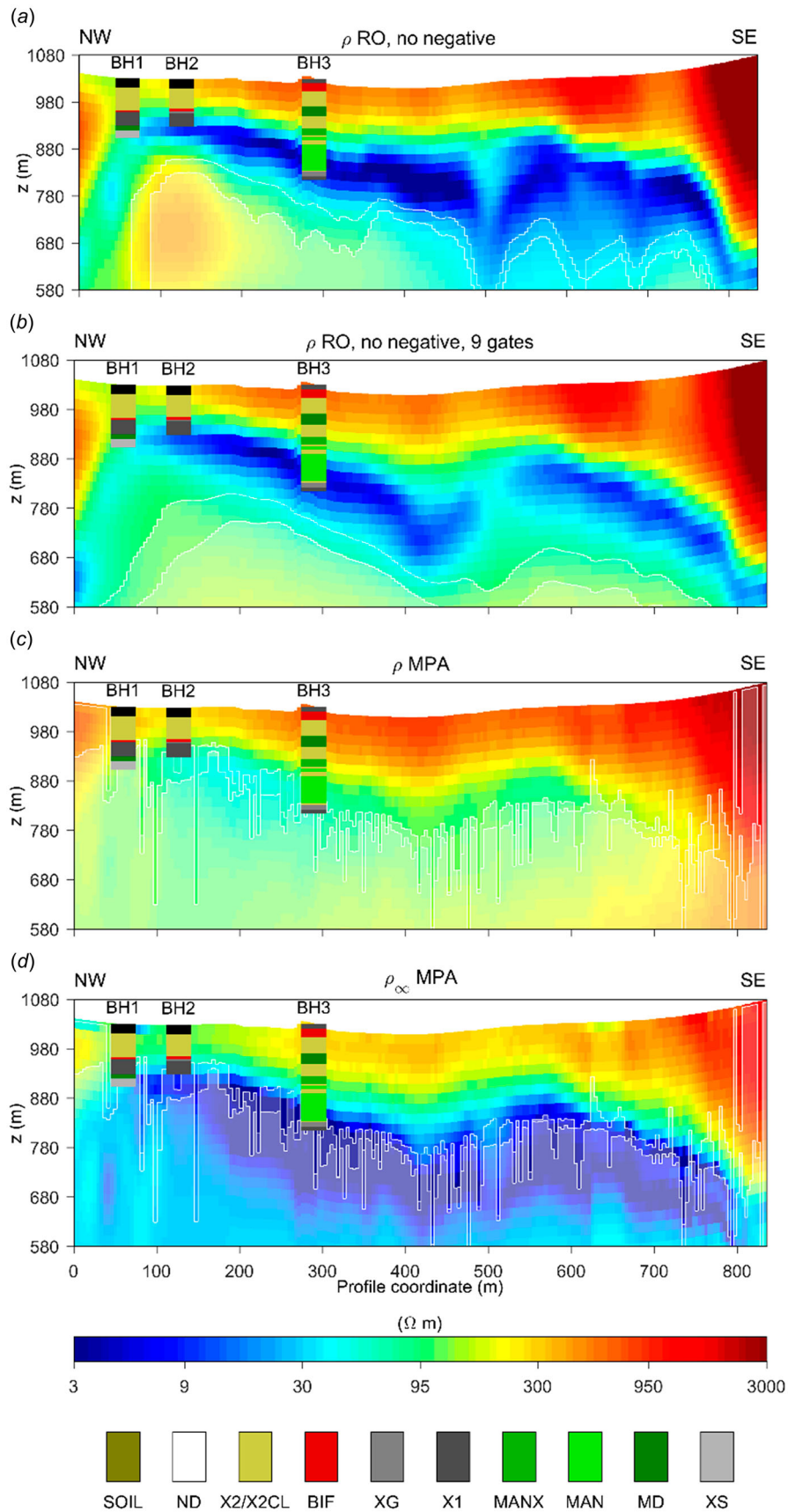


Figure 7. Comparison between the RO and MPA resistivity sections for flight line L20810 with (a) all positive data RO model, (b) the first nine positive gates RO model, (c) ρ_0 MPA model and (d) ρ_∞ MPA model.

IP effect might be removed from the data and, consequently, a more reliable resistivity model might be retrieved by the RO inversion (at least for the shallower layers). However, this is not the case, as shown in Figures 7, in which two RO inversions are compared: the one with all positive-only data (Figure 7(a), as in Figure 5(a)), and the inversion obtained only with the first nine gates (Figure 7(b)). The two RO resistivity models are similar both in terms of resistivity ranges and patterns, and they both differ from MPA resistivity model (Figure 7(c), as in Figure 6(b)). These results indicate that the IP effect is present in the early/intermediate times, which hinders its removal from the data by culling out the late times.

Another concern regarding the comparison of RO and MPA resistivity sections presented so far is that the ρ_0 MPA section represents the DC resistivity, but a significant change in resistivity occurs over frequencies in the Cole–Cole model when high chargeability values are present. Figure 7(d) presents the ρ_∞ section in comparison with the ρ_0 section (Figure 7(c)). As expected, it can be noted that the background value for ρ_∞ is smaller than the one for ρ_0 . However, both models present similar structural behaviour for the shallower and the deeper depth values, in better agreement with the borehole shallower data (the micaceous metapelite – X2/X2CL in the resistivity model sections) than the RO inversions, with no resistive bottom layers coming up as in the RO models, suggesting again that the IP effect plays an important role in the dataset and should be considered in order to recover a more reliable resistivity model.

The discrepancies between the MPA and RO inversion models can be further investigated by focusing on

the 1D resistivity model plots for two sounding positions (soundings 19 and 74, position indicated in Figures 5 and 6) on flight line L20810, presented in Figure 8. These soundings show negative values in the late times of the dB/dt curve, similar to the synthetic tests for ϕ_{max} greater than 200 mrad (Figure 4(c) and (d)). The sounding positions along the profile are indicated by the vertical dashed lines in Figures 5 and 6. In these plots, the inversion results of three-layer models are also shown together with smooth layer inversions.

LCI inversions for the RO parameterisation resulted in resistivity models with thinner and more conductive intermediate layer, compared to all MPA results. In addition, the bottom of the conductive layer and the DOI for the RO models are shallower than for all MPA results, as predicted in the synthetic study. The presence of the negative transients above the noise level and the change in the slope of the dB/dt curve along the anomaly over the Lamego structure and the discrepancies of the resistivity models are all strong indications that a significant IP effect occurs in this region.

This effect maps into the strong chargeable body imaged by the MPA inversion (Figure 6(b)), with ϕ_{max} values between ~ 300 mrad and ~ 450 mrad, and an apparent dip angle of $\sim 25^\circ$ towards SE. This polarisable anomaly is in good agreement with the occurrence of carbonaceous and carbonite schists enriched by carbonaceous material and/or graphite (XC and X1 in borehole legend in Figure 5, respectively) and also with the mafic metapelites that could present sulfides zones (XS in the borehole legend in Figure 5). The structural information recovered from the chargeable body is also in good agreement with the structural control of the the Lamego carbonaceous schist, according to

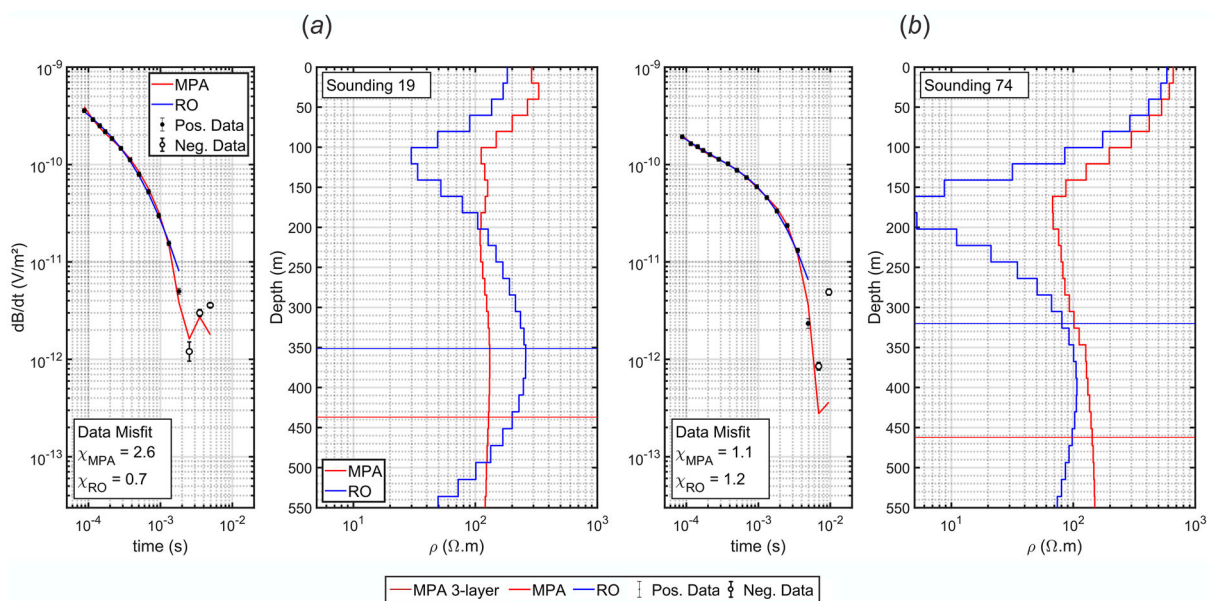


Figure 8. dB/dt curves and 1D resistivity model for RO (blue curves) and MPA (red curves) for (a) Sounding 19 and (b) Sounding 74, which positions along flight line L20810 are indicated in Figures 4 and 5. DOIs are represented by the horizontal continuous lines, according to the models colours.

Martins et al. (2016) who indicated abundant carbonaceous schists in the limbs zones. The limb zones present general dip angle between 20° and 30° to SE and the carbonaceous metapelites layers are associated with S_{1-2} foliation, which presents dip angles between 28° and 42° towards 124° – 134° directions.

In this area, there are no public available ground Spectral IP (SIP) measurements to be compared with these results. For comparison, we briefly discuss Smith et al. (1983) work, which presents laboratory petrophysical measurements for similar carbonaceous schists enriched by graphite and sulfide zones in mafic greenstone belt environment in the Wadi Bidah District, Saudi

Arabia. Their carbonaceous samples presented mean resistivity-values around $300 \Omega \text{ m}$ (range from 17 to $100000 \Omega \text{ m}$), phase values that could reach more than 200 mrad in the range of 100–1000 Hz (the operation range of the AeroTEM^{HD} survey presented in this paper), but with ϕ_{max} values of the order 400–450 mrad around 2.0 Hz and associated τ_ϕ around 8 ms for the most resistive samples. However, even though the frequency range for the IP effect in the AeroTEM^{HD} system is different from the one used in Smith et al. (1983) measurements (Zonge Engineering GDP-12, which results were presented in the frequency range 0.06–1024 Hz), one of the advantages of using the MPA parameterisation is

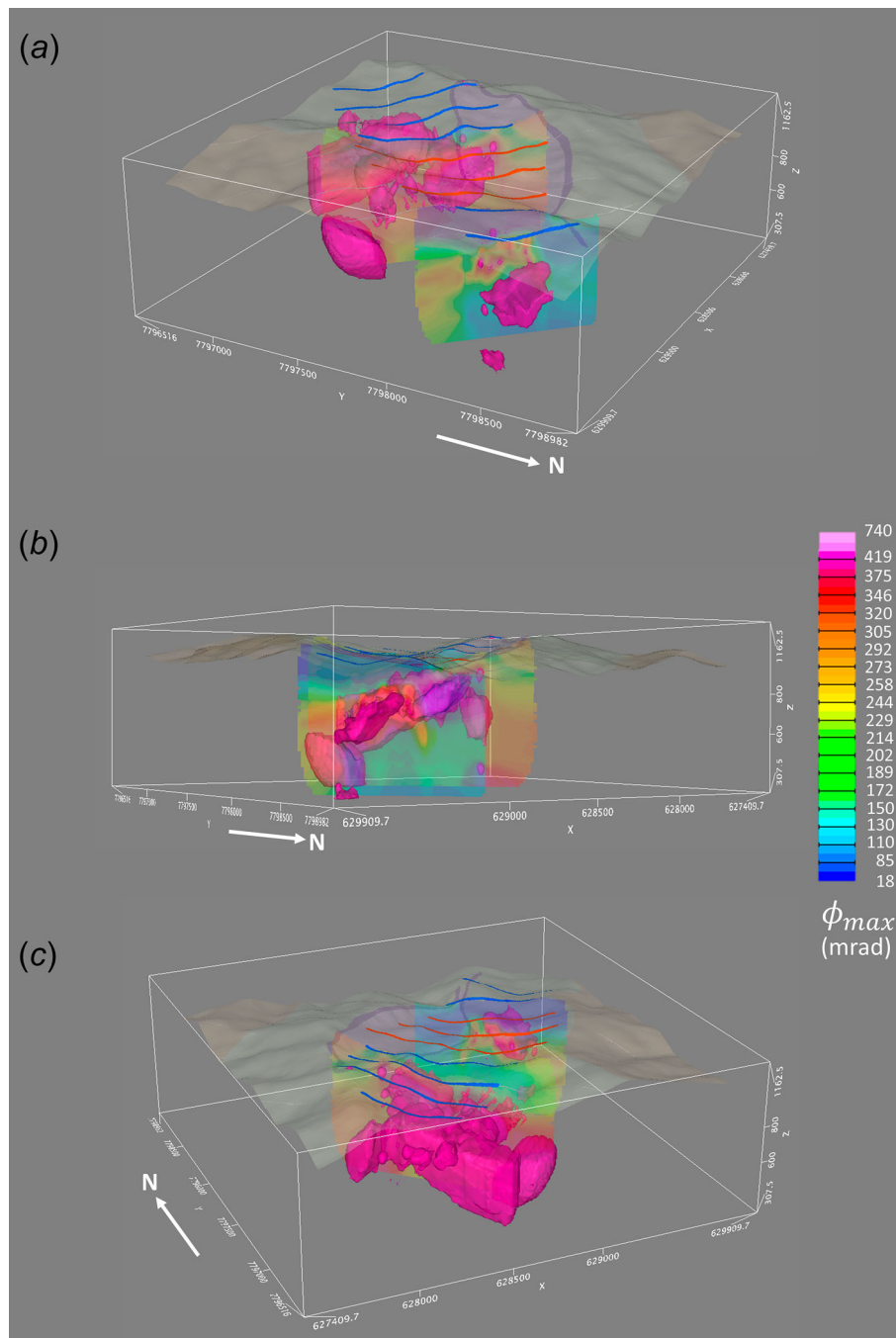


Figure 9. 3D view of the polarisable body through the interpolation of all inverted flight-line intervals (blue lines). (a) Looking to SW upper view. (b) Looking to SW lateral view. (c) Looking to NE upper view. The white arrow indicates the North. The surface represents the geological map as presented in Figure 1 with the digital terrain model relief.

that the inversion looks for the maximum phase value, which makes the comparison easier. The ϕ_{\max} and τ_{ϕ} distributions recovered in this work (Figure 6(b) and (c), respectively) present maximum values up to 450 mrad in the inner portions of the polarisable body and τ_{ϕ} up to 8 ms over the top this polarisable body. These values are compatible with the ones presented in Smith et al. (1983) for the carbonaceous lithologies, including their most resistive samples.

These results suggest that the MPA inversion approach was capable to map the zones of the top of the carbonaceous schist layer, which play an important role in the structural control of the gold mineralisation in the Lamego mine (Martins et al. 2016).

Figures 6(c) and (d) present the MPA LCI sections for τ_{ϕ} and C , respectively. For the τ_{ϕ} section, the DOI is mainly close to the surface except at a few sounding positions at which more (negative) data are present, which implies that the parameter is not well resolved in the inversion, especially when positive-only data exist. On the other hand, the C coefficient is well resolved with values around 0.5, indicating that a Cole–Cole like spectral behaviour is preferred by the inversion (and not a constant spectrum, which would correspond to C values around or below 0.1).

Figure 9 presents the general view of the spatial distribution of the polarisable body for all inverted flight-line intervals over the Lamego structure (blue lines in Figure 1), integrated with the geological map. The 3D volume of ϕ_{\max} was created by inverse distance interpolation of the 2D MPA models. The high chargeability body is defined by a 400 mrad threshold. Figure 9 show two 3D views from different orientations: looking to SW upper view (Figure 9(a)), to SW lateral view (Figure 9(b)) and to NE upper view (Figure 9(c)). In the view to NE, the polarisable body becomes thicker nearby the hinge zone of the structure, suggesting that the carbonaceous schist and graphite enriched layers is thickened, as discussed in Martins et al. (2016). The view to NW presents a steeper dip of the polarisable body mapped in the NE portion, the limbs junction zone, estimated around 45°–50° towards SE along the flight line direction (N45W), which is also in good agreement with the values presented Martins et al. (2016).

Discussion

The results from MPA and RO inversions present several differences, indicating that the presence of the IP phenomenon in this AeroTEM^{HD} survey is significant over the Lamego mine area. These results are in good agreement with the synthetic study which demonstrated that the sensitivity to the IP parameters is significant not only for time values around the sign change and in the negative transients, but also in the positive part of the decay. Consequently, removing the negative data and carrying out a RO inversion could not be the best approach when

dealing with IP-affected responses. In our example this would lead to a non-realistic resistivity model and to wrong interpretation of the conductor associated with the host rocks, like the carbonaceous/graphite. On the other hand, the MPA models had the capability of fitting negative data and a much better agreement with the borehole data. The depths of the top of the shallow resistive and non-polarisable layer associated with the micaceous schist and the top of the conductive and polarisable layer associated with the carbonaceous schist are in better agreement with the borehole profiles for the MPA model (Figure 6(a) and (b)), than for the RO results (Figure 5(a)). However, the MPA modelling increases significantly the size of the model space, and it is significantly more sensitive than the RO inversion to the starting model. In this study, this limitation was addressed using ancillary information, as the laboratory spectra measured on similar lithologies, for guessing the starting values of the IP parameters.

In addition, it is worth mentioning that the classical Cole–Cole model inversions using the same 1D laterally constrained robust inversion scheme were tried, but not presented in this work. The resistivity and chargeability models of the classic Cole–Cole inversions still presented better agreement with the geological data than the RO parameterisation, but the MPA results presented even better agreement and data misfit and are easier to compare to laboratory spectra.

In other areas of the QF region and also in other surveys conducted with AeroTEM^{HD} or other low moment systems, it is possible to have zones where the AEMIP phenomenon is not very clear or only present few negative transients. However, the results presented in this paper indicate that in areas with expected polarisable anomalies, significant changes in the slope of the dB/dt curve could indicate the occurrence of IP effects. Finally, a remark about the ϕ_{\max} range that gives significant IP effects in the data in the synthetic and field examples presented in this study. The low limit of ϕ_{\max} values that affected the data significantly, down to a few tens of mrad, depends on the high resistivity of the background model. In more conductive environments, higher ϕ_{\max} values are needed for a significant IP affect in the TEM responses.

Conclusions

An AeroTEM^{HD} survey was conducted over the Lamego mine area and the data were inverted with RO and MPA robust inversion scheme using the AarhusInv code. The MPA inversion approach with the robust scheme agreed better with the borehole data, and gave more reliable resistivity models than the RO inversion. In particular, the MPA inversions were able to provide a more reliable image of the carbonaceous schists/graphite enriched metapelites layers and/or the sulfide mafic units.

In addition, the ϕ_{\max} model resulting from MPA inversion, allowed to distinguish the chargeable units that could be associated with the carbonaceous layers. The structural behaviour of the polarisable body presents good agreement with the known dip and direction angles for the Lamego structure, and the ϕ_{\max} values present good agreement with petrophysical measurements for similar lithologies in a greenstone belt environment. These results indicate that the MPA robust inversion scheme is reliable inversion procedure for inverting the IP-affected airborne TEM data in case of mineralizations associated with metallic sulfides and chargeable unities with carbonaceous content.

Acknowledgments

The authors also would like to thank CPRM – Geological Survey of Brazil, who provided the AeroTEM^{HD} and geological data, AngloGold Ashanti, who provided the borehole and petrophysical data. In particular, Marco Antonio Couto Junior also would like to thank CPRM researcher Rayanni Caroline Ramos Ferreira for the discussions about Lamego geology, which was essential for the interpretation of these results.

Disclosure statement

No potential conflict of interest was reported by the authors.

Funding

This study was financed in part by the Coordenação de Aperfeiçoamento de Pessoal de Nível Superior - Brasil (CAPES) - Finance Code 001. Jorge Luis Porsani would also like to thank CNPq-Conselho Nacional de Desenvolvimento Científico e Tecnológico for fellowship (grants: 303731/ 2017-6).

ORCID

Marco Antonio Couto Junior  <http://orcid.org/0000-0002-5747-1474>

Anders Vest Christiansen  <http://orcid.org/0000-0001-5829-2913>

Esben Auken  <http://orcid.org/0000-0002-5397-4832>

References

- Auken, E., A.V. Christiansen, G. Fiandaca, C. Schamper, A.A. Behroozmand, A. Binley, E. Nielsen, et al. 2015. An overview of a highly versatile forward and stable inverse algorithm for airborne, ground-based and borehole electromagnetic and electric data. *Exploration Geophysics* 46: 223–35.
- Auken, E., A.V. Christiansen, J.A. Westergaard, C. Kirkegaard, N. Foged, and A. Viezzoli. 2009. An integrated processing scheme for high-resolution airborne electromagnetic surveys, the skytem system. *Exploration Geophysics* 40: 184–92.
- Fiandaca, G., A. Christiansen, and E. Auken. 2015. Depth of investigation for multi-parameters inversions. *Near Surface Geoscience 2015-21st European Meeting of Environmental and Engineering Geophysics*.
- Fiandaca, G., C. Lin, E. Auken, and A. Christiansen. 2018a. *Robust inversion of induced polarization effects in airborne transient electromagnetic*. AEM2018 – 7th International Workshop on airborne electromagnetics – Extended Abstracts.
- Fiandaca, G., L.M. Madsen, and P.K. Maurya. 2018b. Re-parameterizations of the Cole-Cole model for improved spectral inversion of induced polarization data. *Near Surface Geophysics* 16: 385–99.
- Gisselø, P.G., and N.S. Nyboe. 2018. *Optimized for depth of investigation*. Aem2018 – 7th International Workshop on airborne electromagnetics. AEM2018 – 7th International Workshop on airborne electromagnetics – Extended Abstracts.
- Kaminski, V., and A. Viezzoli. 2017. Modeling induced polarization effects in helicopter time-domain electromagnetic data: Field case studies. *Geophysics* 82: B49–61.
- Kang, S., D. Fournier, and D.W. Oldenburg. 2017. Inversion of airborne geophysics over the Do-27/Do-18 Kimberlites – Part 3: Induced polarization. *Interpretation* 5: T327–40.
- Kang, S., and D.W. Oldenburg. 2016. On recovering distributed Ip information from inductive source time domain electromagnetic data. *Geophysical Journal International* 207: 174–96.
- Kratzer, T., and J. Macnae. 2012. Induced polarization in airborne Em. *Geophysics* 77: E317–27.
- Lin, C., G. Fiandaca, E. Auken, M.A. Couto, and A. Christiansen. 2019. A discussion of 2d induced polarization effects in airborne electromagnetic and inversion with a robust 1d laterally constrained inversion scheme. *Submitted to Geophysics*.
- Macnae, J. 2016. Quantifying airborne induced polarization effects in helicopter time domain electromagnetics. *Journal of Applied Geophysics* 135: 495–502.
- Marchant, D., E. Haber, and D. Oldenburg. 2014. Three-dimensional modeling of Ip effects in time-domain electromagnetic data. *Geophysics* 79: E303–14.
- Martins, B.d.S., L.M. Lobato, C.A. Rosière, S.G. Hagemann, J.O.S. Santos, F.L.d.S.P. Villanova, R.C. Figueiredo e Silva, and L.H. de Ávila Lemos. 2016. The Archean Bif-Hosted Lamego gold deposit, Rio Das Velhas greenstone belt, Quadrilátero Ferrífero: Evidence for Cambrian structural Modification of an Archean orogenic gold deposit. *Ore Geology Reviews* 72: 963–88.
- Pelton, W.H., S.H. Ward, P.G. Hallof, W.R. Sill, and P.H. Nelson. 1978. Mineral discrimination and removal of Inductive coupling with Multifrequency Ip. *Geophysics* 43: 588–609.
- Seigel, H.O. 1959. Mathematical Formulation and type curves for induced polarization. *Geophysics* 24: 547–65.
- Smith, B.D., C. Tippens, V. Flanigan, and H. Sadek. 1983. Preliminary results of spectral induced polarization measurements, Wadi Bidah District, Kingdom of Saudi Arabia. *US Geological Survey, Open-File Report*, 83–612.
- Viezzoli, A., G. Fiandaca, and S. Sergio. 2013. Study on the potential of recovering Ip parameters from airborne tem data in layered geology. 6th International AEM Conference & Exhibition.
- Viezzoli, A., V. Kaminski, and G. Fiandaca. 2017. Modeling induced polarization effects in helicopter time domain electromagnetic data: Synthetic case studies. *Geophysics* 82: E31–50.
- Viezzoli, A., V. Kaminskiy, N. Ebner, and A. Menghini. 2016. *Extracting Ip information from aem data to improve the hydrogeological interpretation*. ASEG-PESA-AIG 2016.